BLACK SILICON FABRICATED BY SILVER-ASSISTED CHEMICAL ETCHING FOR FLEXIBLE SOLAR CELLS

HALO DALSHAD OMAR

UNIVERSITI SAINS MALAYSIA

2023

BLACK SILICON FABRICATED BY SILVER-ASSISTED CHEMICAL ETCHING FOR FLEXIBLE SOLAR CELLS

by

HALO DALSHAD OMAR

Thesis submitted in fulfilment of the requirements
for the degree of
Doctor of Philosophy

March 2023

ACKNOWLEDGEMENT

Firstly, thanks to Allah for giving me a chance to complete this research and thesis. I would like to express my deepest appreciation and thanks to my main supervisor, Ts. Dr. Mohd Zamir Pakhuruddin, for providing me with the opportunity to pursue this research under his supervision and all the kind guidance and support he provided. Thank you for inspiring me in this scientific pursuit. I would also like to express my thanks to my co-supervisor, Professor Dr. Md. Roslan Hashim for his suggestions and guidance during my PhD.

Thanks to School of Physics, Universiti Sains Malaysia (USM) and Ministry of High Education (MoHE) of Malaysia. Again, thanks to Universiti Sains Malaysia (USM) for funding this research through Short-Term Grant 304/PFIZIK/6315063. Much of this work would have been virtually impossible without the technical supports from Nano-Optoelectronics Research and Technology Laboratory (NOR) staffs; Mrs. Ee Bee Choo, Mr. Abdul Jamil Yusuf, Mrs. Aznorhaida Ramli and Mr. Yushamdan Yusof, and others (not mentioned here) who have given me useful advices throughout this research. I would like to thank, Department of Physics, Faculty of Science and Health, Koya University and Ministry of Higher Education and Scientific Research-Kurdistan Iraq.

My deepest appreciations are expressed to my lovely father and my lovely mother. Finally, I would like to thank my dearest wife, Sara for her constant motivation. Not to forget my beloved children; Daban and Darin for cherishing my life all this while. Heartfelt thanks and greatest appreciation go to all my relatives and friends for their continuous support during my studies.

TABLE OF CONTENTS

ACKNOWLEDGEMENT ..... **ii**

TABLE OF CONTENTS ..... **iii**

LIST OF TABLES ..... **vi**

LIST OF FIGURES ..... **viii**

LIST OF SYMBOLS ..... **xv**

LIST OF ABBREVIATIONS ..... **xvi**

ABSTRAK ..... **xix**

ABSTRACT ..... **xxi**

CHAPTER 1 INTRODUCTION **1**

1.1 Introduction 1

1.2 Problem statement 5

1.3 Objectives of research 7

1.4 Thesis outline 7

CHAPTER 2 THEORETICAL BACKGROUND AND LITERATURE REVIEW…… **9**

2.1 Introduction 9

2.2 Solar irradiation 9

2.3 Flexible monocrystalline silicon solar cells 11

2.4 Optical properties of flexible monocrystalline silicon 12

2.5 Light management in flexible monocrystalline silicon solar cells 16

2.6 Black silicon 17

2.7 Fabrication of black silicon 20

2.8 Metal-assisted chemical etching (MACE) 23

2.8.1 One-step and two-step MACE processes 24

2.8.2 Types of catalyst in MACE process 26

2.9 Fabrication of flexible black silicon solar cell 28
2.9.1 Homojunction solar cell 28
2.9.2 Heterojunction solar cell 30
2.10 Electrical properties of solar cells 33
2.10.1 Current-voltage characteristics 33
2.10.2 Fill factor 34
2.10.3 Conversion efficiency 34
2.10.4 Quantum efficiency 34
CHAPTER 3 EXPERIMENTAL DETAILS 36
3.1 Introduction 36
3.2 Fabrication of flexible monocrystalline silicon 38
3.3 Radio Corporation of America cleaning 40
3.4 Fabrication of flexible black silicon by MACE process 41
3.5 Fabrication of heterojunction flexible black silicon solar cell 42
3.6 Metallization of flexible black silicon solar cell 43
3.7 Surface texturing of stainless steel substrate 46
3.8 Surface texturing of polyimide substrate 47
3.9 Characterizations of flexible black silicon, textured stainless steel and textured polyimide substrates 50
3.9.1 Surface morphological properties 50
3.9.2 Structural properties 52
3.9.3 Optical properties 53
3.10 Electrical characterizations of flexible black silicon solar cell 55
3.10.1 Hall effect measurement system 56
3.10.2 Current-voltage characteristics 56
CHAPTER 4 RESULTS AND DISCUSSION 58
4.1 Introduction 58
4.2 Effects of etching time 58

4.2.1 Surface morphological properties 59
4.2.2 Optical properties 64
4.3 Effects of etchant volume ratio 69
4.3.1 Surface morphological properties 69
4.3.2 Optical properties 71
4.4 Properties of flexible black silicon on untextured stainless steel substrate 75
4.4.1 Optical properties 76
4.5 Properties of flexible black silicon on textured stainless steel substrate 80
4.5.1 Surface morphological properties 81
4.5.2 Structural properties 85
4.5.3 Optical properties 85
4.6 Properties of flexible black silicon on textured polyimide substrate 92
4.6.1 Surface morphological properties 92
4.6.2 Structural properties 97
4.6.3 Optical properties 97
4.7 Properties of PEDOT:PSS emitter on heterojunction flexible black silicon 104
4.7.1 Surface morphological properties 105
4.7.2 Optical properties 106
4.7.3 Electrical properties 110
4.8 Electrical characterization of heterojunction flexible black silicon solar cells on polyimide substrate 111
CHAPTER 5 CONCLUSION AND RECOMMENDATIONS 114
5.1 Conclusion 114
5.2 Original contributions 116
5.3 Recommendations for future studies 118
REFERENCES 119
LIST OF PUBLICATIONS

LIST OF TABLES

Page

Table 2.1 Relationship between AM and zenith angle.....11

Table 3.1 Properties of silver epoxy adhesive.....47

Table 4.1 Potential $J_{sc(max)}$ and $J_{sc(max)}$ enhancement of flexible b-Si with different etching duration (5–25 min) compared to the flexible c-Si wafer (reference).....68

Table 4.2 Summary of morphological and optical properties for the wafers with varying etching time.....69

Table 4.3 Potential $J_{sc(max)}$ of flexible b-Si wafers after being etched in different etchant concentrations. 74

Table 4.4 Summary of morphological and optical properties for the wafers with varying H_2O_2 ratio.....74

Table 4.5 Potential $J_{sc(max)}$ and $J_{sc(max)}$ enhancement of flexible b-Si on SS substrate formed by varying etching times (10-25 min) during MACE process. Potential $J_{sc\ (max)}$ of planar c-Si on SS substrate is used as a reference. 79

Table 4.6 Summary of optical properties for the wafers with varying etching times. 80

Table 4.7 Potential $J_{sc(max)}$ of flexible b-Si (flexible b-Si produced by MACE process for 20 min of etching time) on untextured SS and textured SS substrates. 91

Table 4.8 Summary of morphological and optical properties for the SS substrates with varying etching time.....91

Table 4.9 Elements detected (in atomic %) on textured PI substrate.....94

Table 4.10 Summary of potential $J_{sc(max)}$ of flexible b-Si on untextured and textured PI substrates. $J_{sc(max)}$ enhancement (%) is derived by normalizing the improved $J_{sc(max)}$ of the flexible b-Si wafer on

textured PI substrate over the potential $J_{sc(max)}$ of the flexible b-Si on untextured PI substrate. 102

Table 4.11 Summary of morphological and optical properties for the PI substrates with varying annealing time. 103

Table 4.12 Summary of AWR (within 300-1100 nm wavelength region) and potential $J_{sc(max)}$ of flexible b-Si (after 20 min of etching process) on both untextured and textured SS and PI substrates. Note that the thickness for all the flexible b-Si is 65 μm with (100) orientation and p-type are used in this work. 104

Table 4.13 Potential $J_{sc(max)}$ of PEDOT:PSS/flexible c-Si and PEDOT:PSS/flexible b-Si on untextured and textured PI substrates. Potential $J_{sc(max)}$ of PEDOT:PSS/flexible c-Si on untextured PI substrates is used as a reference. 110

Table 4.14 Summary of electrical properties of PEDOT:PSS on flexible c-Si and b-Si as measured by Hall effect system. 111

Table 4.15 Summary from J-V characteristics of the PEDOT:PSS/flexible c-Si and PEDOT:PSS/flexible b-Si solar cells and both cells are on untextured and textured PI substrates. 113

LIST OF FIGURES

Page

Figure 1.1 Fossil fuels dominate world's energy system (Sharma et al., 2021). 1

Figure 1.2 The ITRPV price trend of c-Si solar modules in US$/Watt$_p$ (ITRPV, 2022). 2

Figure 1.3 National Renewable Energy Laboratory (NREL's) best research solar cell efficiencies for different technologies, since 1975 (NREL, 2022).....4

Figure 2.1 Spectrum irradiance for the standardized solar spectra. The figure is adopted by National Renewable Energy Laboratory (NREL) (NREL, 2022).....10

Figure 2.2 Flexible device on a plastic substrate that ensures mechanical stability (Zhang et al., 2022). 12

Figure 2.3 Path of the incident light upon incidence (left) planar c-Si (180 μm thickness) and (right) planar c-Si (65 μm thickness). Note that the diagrams are not to scale. 13

Figure 2.4 Transmission spectra of c-Si wafers with thicknesses of t_{Si}=6.8, 14.8, 49.4, and 200 μm (Dai et al., 2019). 14

Figure 2.5 E-k diagram of c-Si (Yuan et al., 2018). 14

Figure 2.6 Absorption coefficient and absorption depth of c-Si at 300 K (Hwang et al., 2018).....15

Figure 2.7 (a) Planar c-Si wafer (b) black silicon wafer (Zhang et al., 2020) (c) schematic diagram of b-Si NWs in the corresponding effective refractive index (n_{eff}) when the incident light travels from air (n=1) into bulk c-Si (n=3.94) (Katiyar et al., 2015).....18

Figure 2.8 Schematic diagram of Al_2O_3 surface passivation on b-Si solar cell (Wang et al., 2013).....20

Figure 2.9 Cross-sectional schematic diagrams of the b-Si using different fabrication techniques such as (a) RIE process in an atmosphere of SF_6 and O_2 (b) needle-shaped structures by femtosecond laser pulses (c) macroporous Si fabrication by electrochemical etching (d) MACE process with Ag/Au catalyst NPs in aqueous HF and hydrogen peroxide (H_2O_2) solution (not to scale) (Otto et al., 2015). 21

Figure 2.10 (a) Energy level diagram of c-Si substrate in contact with an aqueous solution containing $AgNO_3$:HF (b) schematic illustration of c-Si nanowires formed by one-step of MACE process.....26

Figure 2.11 Schematic diagram of various metal catalyst on the depth of pores formation on the c-Si surface (Alhmoud et al., 2021). 27

Figure 2.12 The energy band diagram of a p-n homojunction at thermal equilibrium condition. 29

Figure 2.13 Schematic diagram of a homojunction b-Si solar cell. 29

Figure 2.14 Schematic of energy level diagram of PEDOT:PSS/n-type c-Si heterojunction solar cell with work function value for Ag, E_{LUMO} and E_{HOMO} values for PEDOT:PSS, conduction and valence band energy for c-Si. 31

Figure 2.15 Schematic diagram of a heterojunction b-Si solar cell.....32

Figure 2.16 Current-voltage characteristics of a solar cell under illumination (Ushasree and Bora, 2019). 33

Figure 2.17 External quantum efficiency plot for a solar cell (Honsberg and Bowden, 2010). 35

Figure 3.1 Flow chart for fabrication and characterizations of flexible b-Si and heterojunction b-Si solar cell.....37

Figure 3.2 Technique used in temperature stabilization. 39

Figure 3.3 Image of flexible c-Si wafer with a thickness of about 65 μm. 40

Figure 3.4 (a) Flexible c-Si wafer (b) flexible c-Si after dipped on aqueous solution $AgNO_3$:HF:DI H_2O (7:9:34 ml) by one-step MACE

process (c) flexible b-Si wafer after removal of Ag NPs by HNO_3 for 5 min at room temperature. 42

Figure 3.5 Spin coater (Model: SCS G3P spin coater) and schematic of the spin coating process. 43

Figure 3.6 Thermal evaporator used to deposit Ag for front and back contacts.....43

Figure 3.7 Schematic diagram of thermal evaporation technique (Martín-Palma and Lakhtakia, 2013).....44

Figure 3.8 The flexible b-Si wafer after Ag front contact evaporation, designed by a shadow mask. 45

Figure 3.9 (a) Untextured SS (b) textured SS substrate with 180 μm thickness used in this work. 46

Figure 3.10 (a) Untextured PI (b) textured PI substrate with 75 μm thickness used in this work. 48

Figure 3.11 The Edwards Auto 500 sputtering technique. 49

Figure 3.12 (a) AFM system (Model: Dimension Edge, Bruker) used to scan the 3D topography of the samples. (b) principle of AFM operation.....51

Figure 3.13 (a) FESEM (Model: FEI Nova NanoSEM 450) (b) schematic diagram of basic working principle of FESEM system (Jusman et al., 2014). 52

Figure 3.14 HR-XRD system. 53

Figure 3.15 UV-Vis-NIR spectrophotometer (Model: Cary 5000 by Agilent Technologies) used to measure reflection and transmission of a sample. 54

Figure 3.16 Schematics of (a) specular and (b) diffuse reflections. 54

Figure 3.17 Hall effect measurement system (Model: Accent-HL 5500 PC). 56

Figure 3.18 Solar simulator that is used for J-V measurement of solar cells. 57

Figure 3.19 The comparison of emission spectrum of an AM 1.5G solar simulator spectra and white LED (Yan et al., 2020).....57

Figure 4.1 Images of p-type (100) b-Si wafers after being etched by one-step MACE process with different etching durations: (a) planar c-Si (reference), (b) 5 min, (c) 10 min, (d) 15 min, (e) 20 min, (f) after 25 min and (g) flexible b-Si wafer. 59

Figure 4.2 AFM images of flexible b-Si wafers after being etched by one-step MACE process with different etching durations (a) planar c-Si (reference) (b) 5 min (c) 10 min (d) 15 min (e) 20 min and (f) 25 min. 61

Figure 4.3 (a–e) Top and (f–j) oblique (at 30^{o} tilt angle) view FESEM images of the flexible b-Si NWs with different etching durations (5–25 min). All images include scale bar with 1 μm length. 63

Figure 4.4 (a) Cross-sectional FESEM images of flexible c-Si wafer (reference) with 65 μm thickness and (b–f) flexible b-Si surface formed by different etching durations (5–25 min) during MACE process. The scale bar for (a) image is 100 μm length and (b–f) images are 1 μm length. 64

Figure 4.5 (a) Total reflectance (b) transmission and (c) absorption profiles of thin b-Si wafers with different etching durations (5-25 min). Planar c-Si wafer (unetched) is used as a reference. 66

Figure 4.6 Average length of flexible b-Si NWs and corresponding AWR with different etching durations. Note that the AWR for flexible c-Si reference is 43.6%. 67

Figure 4.7 Oblique (at 30^{o} tilt angle) view FESEM images of flexible b-Si formed by using different etchant concentrations H_2O_2 (1, 2 and 3 ml by volume ratio) for 20 min at room temperature. The scale bar indicates 1 μm. 70

Figure 4.8 Cross-sectional FESEM images of flexible b-Si wafer (a) without H_2O_2 and (b-d) b-Si NWs fabricated with different volume ratios

(1–3 ml) by one-step MACE process. The scale bar indicates 1 μm. 71

Figure 4.9 (a) Reflection, (b) transmission and (c) absorption curves of b-Si wafers by using different etchant concentrations H_2O_2 (1, 2 and 3 ml by volume ratio) for 20 min at room temperature.....73

Figure 4.10 Image of flexible b-Si on flexible SS substrate.....75

Figure 4.11 Cross-sectional FESEM images of flexible b-Si on SS substrate.....76

Figure 4.12 (a) Total reflection and (b) absorption profiles of flexible b-Si (65 μm thickness) surface formed by varying etching times (10-25 min) during MACE process. Planar c-Si reference on untextured SS substrate is included for comparison. 78

Figure 4.13 Schematic diagrams of flexible b-Si on untextured (left) and textured (right) SS substrates. Path of the incident light in both cases are illustrated. Note that the diagrams are not to scale. 81

Figure 4.14 Oblique (30^o) FESEM images for (a) untextured SS substrate surface and textured SS substrates using HF solution with different etching durations; (b) 10 min (c) 20 min (d) 30 min. The scale bars represent 1 μm. 82

Figure 4.15 AFM images of (a) untextured SS substrate and textured SS substrates using HF solution with different etching durations; (b) 10 min (c) 20 min (d) 30 min. 83

Figure 4.16 (a) RMS roughness and (b) texture angle distribution of SS substrates after being textured at different durations (10-30 min) in HF acid. Untextured SS substrate is used as a reference. 84

Figure 4.17 XRD profiles of the untextured and textured SS substrates at different etching durations (10-30 min). 85

Figure 4.18 (a) Diffuse (b) specular and (c) total reflection curves of textured SS substrates with different etching times (10-30 min) for the wavelength range of 800-1100 nm. Untextured SS substrate is also provided for comparison. 87

Figure 4.19 (a) Total reflection (with corresponding AWR values shown in the legends) and (b) absorption profiles of flexible b-Si on untextured and textured SS substrates for different etching durations (10-30 min) (c) Total reflection curves for 800-1100 nm spectral region (d) absorption curves for 800-1100 nm spectral region. 89

Figure 4.20 Absorption enhancement curves of flexible b-Si on textured SS substrates for different etching durations. 90

Figure 4.21 Image of flexible b-Si on flexible PI substrate.....92

Figure 4.22 Oblique (30^o tilt angle) FESEM images for, (a) untextured PI substrate and textured PI substrate with varying annealing times; (b) 60 min, (c) 90 min, (d) 120 min. The scale bar indicates 1 μm. ..93

Figure 4.23 EDX spectra of textured PI (after Cu removal) substrate. 94

Figure 4.24 AFM images of (a) untextured PI substrate and textured PI substrates after being annealed for (b) 60 min (c) 90 min (d) 120 min. 95

Figure 4.25 (a) RMS surface roughness and (b) texture angle distribution on PI substrate, after annealing with different durations (60–120 min), calculated from AFM measurement. Untextured PI substrate is shown as a reference. 96

Figure 4.26 XRD profiles of the untextured and textured PI substrates with different annealing durations (60-120 min). 97

Figure 4.27 (a) Diffuse (b) specular and (c) total reflection profiles of textured PI substrates with varying annealing durations (60-120 min) for the wavelength range of 800-1100 nm. Untextured PI substrate is also provided for comparison. 98

Figure 4.28 (a) Total reflection and (b) absorption curves of flexible b-Si on untextured and textured PI substrates for varying annealing durations (60-120 min) (c) total reflection curves for 800-1100 nm spectral region (d) absorption curves for 800-1100 nm spectral region. 100

Figure 4.29 Light absorption enhancement profiles of flexible b-Si on textured PI substrates for varying annealing times. 101

Figure 4.30 Schematic diagram for fabrication of the flexible PEDOT:PSS/b-Si solar cells on textured PI substrate. 105

Figure 4.31 (a) Oblique (30^o) and (b) cross-sectional view FESEM images of the PEDOT:PSS layer coated on n-type (100) b-Si NWs. 106

Figure 4.32 (a) Total reflection (with corresponding hemispherical AWR values are shown in the legend) and (b) absorption of PEDOT:PSS/flexible b-Si and PEDOT:PSS/flexible b-Si on untextured and textured PI substrates. PEDOT:PSS/flexible c-Si reference and PEDOT:PSS/flexible c-Si reference on untextured and textured PI substrates are shown for comparison (c) total reflection curves for 800-1100 nm spectral region (d) absorption curves for 800-1100 nm spectral region.....108

Figure 4.33 J-V curves of the PEDOT:PSS/flexible c-Si and PEDOT:PSS/flexible b-Si cells and both cells are on untextured and textured PI substrates.....113

LIST OF SYMBOLS

A	Absorption
I	Current
I_{sc}	Short-circuit current
J	Current density
J_{sc}	Short-circuit current density
$J_{sc(max)}$	Maximum potential short-circuit current density
n	Refractive index
P	Power
P_{max}	Maximum power
η	Power conversion efficiency
q	Electron charge
R	Reflection
R_s	Series resistance
$S(\lambda)$	Standard photon density of sunlight
T	Transmission
V	Voltage
V_{oc}	Open-circuit voltage
θ	Zenith angle (for AM calculation)
λ	Wavelength of light

LIST OF ABBREVIATIONS

AFM	Atomic force microscopy
Ag	Silver
$AgNO_3$	Silver nitrate
Al	Aluminum
Al_2O_3	Aluminum oxide
ALD	Atomic layer deposition
AM	Air mass
Ar	Argon
ARC	Anti-reflection coating
a-Si	Amorphous silicon
Au	Gold
AWR	Average weighted reflection
B	Boron
BR	Back reflector
b-Si	Black silicon
CB	Conduction band
CdTe	Cadmium telluride
CIGS	Copper indium gallium diselenide
CO_2	Carbon dioxide
Cr	Chromium
c-Si	Crystalline silicon
Cu	Copper
CuO_2	Copper oxide
CZTS	Copper zinc tin sulfide
DC	Direct current
DI H_2O	Deionized water
DMSO	Dimethylsulfoxide
EG	Ethylene glycol
EQE	External quantum efficiency
IQE	Internal quantum efficiency
Fe	Iron

FF	Fill factor
FESEM	Field emission scanning electron microscopy
H_2	Hydrogen
H_2O	Water
H_2O_2	Hydrogen peroxide
H_2PtCl_6	Hexachloroplatinic
H_3PO_4	Phosphoric acid
$HAuCl_4$	Tetrachloroauric (III) acid
HfO_2	Hafnium dioxide
HCl	Hydrochloric acid
HF	Hydrofluoric acid
HNO_3	Nitric acid
HOMO	Highest occupied molecular orbital
IBC	Interdigitated back-contact
IPA	Isopropyl alcohol
ITRPV	International Technology Roadmap for Photovoltaic
KOH	Potassium hydroxide
LED	Light emitting diode
LUMO	Lowest unoccupied molecular orbital
MACE	Metal-assisted chemical etching
μc-Si	Microcrystalline silicon
N_2	Nitrogen
NaOH	Sodium hydroxide
NH_4OH	Ammonium hydroxide
Ni	Nickel
NP	Nanoparticle
NREL	National Renewable Energy Laboratory
NW	Nanowire
O_2	Oxygen
OH	Hydroxide
Pd	Palladium
P	Phosphorus
P_2O_5	Phosphorus pentoxide
PECVD	Plasma enhanced chemical vapour deposition

PEDOT:PSS	Poly(3,4-ethylenedioxy-thiophene):poly(styrene-sulfonate)
PI	Polyimide
$POCl_3$	Phosphoryl chloride
Pt	Platinum
PV	Photovoltaic
QE	Quantum efficiency
RCA	Radio Corporation of America
RIE	Reactive ion etching
RMS	Root mean square
Sc_2O_3	Scandium oxide
SF_6	Sulphur hexafluoride
SiF_4:O_2	Silicon-oxyfluorine
SiN_x	Silicon nitride
SiO_2	Silicon dioxide
SS	Stainless steel
STC	Standard Test Condition
TMAH	Tetramethyl ammonium hydroxide
TiO_2	Titanium oxide
US$	United States Dollar
USM	Universiti Sains Malaysia
UV-Vis-NIR	Ultraviolet-visible-near infrared
VB	Valence band

SILIKON HITAM DIFABRIKASI OLEH PUNARAN KIMIA BERBANTU PERAK UNTUK SEL SURIA FLEKSIBEL

ABSTRAK

Silikon monohablur (c-Si mono) menguasai lebih daripada 90% daripada pasaran fotovoltan disebabkan oleh kecekapan sel suria yang meningkat, kematangan teknologi dan pengurangan harga kos teknologi. Kini, pembuatan fotovoltan menggunakan sel suria dengan ketebalan 180 μm. Untuk mengurangkan kos teknologi, satu strategi yang berpotensi tinggi ialah dengan mengurangkan ketebalan wafer c-Si ke bawah 100 μm, di mana wafer juga akan menjadi fleksibel. Selain itu, wafer yang lebih nipis akan meningkatkan voltan litar terbuka sel suria kerana pengurangan rekombinasi pukal. Walau bagaimanapun, pengurangan ketebalan wafer ke bawah 100 μm akan menjejaskan penyerapan cahayanya, yang mengurangkan fotoarus daripada sel suria. Selain itu, silikon permukaan rata mempamerkan pantulan jalur lebar yang tinggi sekitar 35% dalam kawasan jarak gelombang 300-1100 nm, yang mengurangkan lagi penyerapan cahaya di dalam c-Si. Untuk meningkatkan penyerapan cahaya di dalam wafer c-Si nipis, silikon hitam (b-Si) menawarkan potensi yang tinggi untuk aplikasi sel suria kerana ia menghasilkan penyerapan cahaya jalur lebar yang superior dalam kawasan panjang gelombang 300-1100 nm. Ini disebabkan oleh kesan penggredan indeks biasan, yang mengurangkan pantulan cahaya jalur lebar dan meningkatkan penggandingan-cahaya ke dalam penyerap silikon. Dalam penyelidikan ini, b-Si fleksibel difabrikasi oleh punaran kimia berbantu logam satu-langkah (MACE) dikaji untuk aplikasi sel suria. Wafer c-Si mono dinipiskan ke bawah 100 μm oleh proses punaran kimia basah. Seterusnya, b-Si nanowayar (NWs) difabrikasi di atas wafer melalui proses MACE,

menggunakan perak (Ag) sebagai mangkin. Daripada proses MACE, punaran 20 min menghasilkan pantulan wajaran purata (AWR) terendah pada 8.6% dan penyerapan cahaya jalur lebar tertinggi dalam kawasan panjang gelombang 300-1100 nm. Apabila b-Si fleksibel dilekatkan di atas substrat keluli (SS) bertekstur (punaran 20 min), AWR ialah pada 8.6%. Di atas substrat poliimida (PI) bertekstur (penyepuhlindapan 90 min), AWR menurun ke 7.9%. Dalam sel suria, PI bertekstur digunakan sebagai substrat disebabkan oleh penyerapan cahaya yang lebih tinggi dalam kawasan panjang gelombang yang lebih panjang. PEDOT:PSS (jenis-p) digunakan sebagai pemancar jenis-p di atas b-Si fleksible jenis-n untuk membentuk sel suria heterosimpang. Pencirian arus-voltan dijalankan menggunakan simulator suria diod pemancar cahaya putih (LED) pada iluminasi input 47 mW/cm^2 pada suhu bilik. Sel suria PEDOT:PSS/c-Si fleksibel atas PI tak bertekstur menunjukkan J_{sc} 7.76 mA/cm^2 dan kecekapan 1.57%. Di atas PI bertekstur, J_{sc} meningkat sebanyak 0.2 mA/cm^2, oleh kerana peningkatan penyerapan cahaya gelombang panjang. Kecekapan sel suria meningkat ke 1.62%. Untuk sel suria PEDOT:PSS/b-Si fleksibel di atas PI tak bertekstur, J_{sc} meningkat 2 mA/cm^2 hasil daripada peningkatan penyerapan cahaya jalur lebar dan kecekapan meningkat ke 2.51%. Dengan PI bertekstur, kecekapan meningkat ke 2.58%, hasil daripada peningkatan penyerapan cahaya atas panjang gelombang 800 nm.

BLACK SILICON FABRICATED BY SILVER-ASSISTED CHEMICAL ETCHING FOR FLEXIBLE SOLAR CELLS

ABSTRACT

Monocrystalline silicon (mono c-Si) dominates more than 90% of photovoltaic market due to increasing solar cell efficiencies, technology maturity and reducing technology cost. Currently, photovoltaic manufacturing uses solar cells with 180 μm thickness. To reduce the technology cost, one promising strategy is by reducing the c-Si wafer thickness below 100 μm, whereby the wafer becomes flexible. Furthermore, flexible c-Si introduces new features including flexibility, light weight and makes thin c-Si highly attractive for flexible solar cells. Most importantly, thin c-Si solar cells usually demonstrate higher open circuit voltage (V_{oc}) due to the lower bulk recombination and more efficient electron-hole pair extraction. However, one big challenge of the thin c-Si is the insufficient light absorption due to the indirect bandgap of the c-Si. Additionally, planar c-Si exhibits a high broadband reflection of around 35% within 300-1100 nm wavelength region, which further reduces the light absorption in the c-Si. To improve the light absorption in the thin c-Si wafers, black silicon (b-Si) offers a great potential for solar cell application since it yields a superior broadband light absorption within 300-1100 nm wavelength region. This is attributed to refractive index (n) grading effect, which reduces broadband light reflection and improves light-coupling into the silicon absorber. In this work, flexible b-Si fabricated by one-step metal-assisted chemical etching (MACE) is investigated for solar cell application. Mono c-Si wafers are thinned down to below 100 μm by a wet chemical etching process. Then, b-Si nanowires (NWs) are fabricated on the wafers using MACE process, utilizing silver

(Ag) as the catalyst. From the MACE process, 20 min etching leads to the lowest average weighted reflection (AWR) of 8.6% and the highest broadband light absorption within the 300-1100 nm wavelength region. When the flexible b-Si is attached on a textured stainless steel (SS) substrate (20 min of etching), the AWR is 8.6%. On a textured polyimide (PI) substrate (90 min of annealing), the AWR reduces further to 7.9%. For solar cell fabrication, the flexible b-Si on textured PI exhibits higher absorption in the long wavelength region. PEDOT:PSS (p-type) is used as the front emitter on the n-type flexible b-Si to form a heterojunction solar cell. Current-voltage characterization is carried out using white light emitting diode (LED) solar simulator at input illumination of 47 mW/cm^2 at room temperature. The PEDOT:PSS/flexible c-Si solar cell on untextured PI illustrates J_{sc} of 7.76 mA/cm^2 and efficiency of 1.57%. On the textured PI, the J_{sc} increases by 0.2 mA/cm^2, due to the improved long wavelength light absorption. Efficiency of the solar cell increases to 1.62%. For the PEDOT:PSS/flexible b-Si on untextured PI, the J_{sc} improves by about 2 mA/cm^2 as a result of the improved broadband light absorption and the efficiency increases to 2.51%. With the textured PI substrate, the efficiency increases to 2.58% due to the increased J_{sc}, owing to the enhanced light absorption above wavelength of 800 nm.

CHAPTER 1

INTRODUCTION

1.1 Introduction

The current major challenge is to solve the growing electricity demand by the increasing world's population (Haegel and Kurtz, 2021). Currently, about 80% of the energy market is dominated by fossil fuels; oil, gas and coal and more than 65% of electricity generation depends on the fossil fuels, as shown in Figure 1.1. However, fossil fuels are known to be the main source of pollution and harmful to the environment due to the emission of greenhouse gases (Abbasi et al., 2022). A promising alternative to fossil fuels is solar energy (Huo et al., 2020). Solar energy is a promising renewable energy source and clean energy (without pollution) on earth. The main advantage of the solar energy is that it is of unlimited sources. A solar cell can absorb photons from the solar irradiation and convert them into electricity. This process is known as photovoltaic (PV) effect (Haegel and Kurtz, 2021).

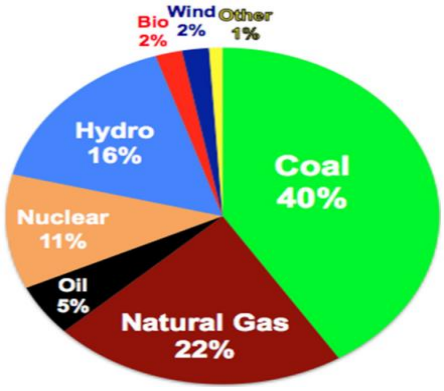

Figure 1.1 Fossil fuels dominate world's energy system (Sharma et al., 2021).

Solar cell technologies are categorized into three generations. The first generation solar cells are based on monocrystalline silicon (mono c-Si) and

multicrystalline silicon (multi c-Si). These technologies still dominate more than 90% of the PV market due to its abundance in the earth's crust, constant technological innovation, increased conversion efficiency, technology maturity, non-toxicity and economies of scale which lead to consistent reduction in technology cost (Cui et al., 2022; Wilson et al., 2020). During the past several decades, the thickness of c-Si wafers has been reduced from 400 µm to currently 180 µm in the PV manufacturing (Andreani et al., 2019; Zhu et al., 2022). Going forward, the reduction of the c-Si wafers thickness to below 100 µm in a thin c-Si solar cell can suppress the technology cost of the PV modules significantly (Liu et al., 2020; Um et al., 2021). According to International Technology Roadmap for Photovoltaic (ITRPV), the price of solar cells has reduced in the last few years and the price is expected that the trend will continue in the coming years. Figure 1.2 illustrates the reduction in c-Si technology cost in US$/Watt$_p$ for the period of 1976-2021 (ITRPV, 2022). To date, the module price for mono c-Si technology has reduced to less than US$0.25/Watt$_p$ (Wilson et al., 2020).

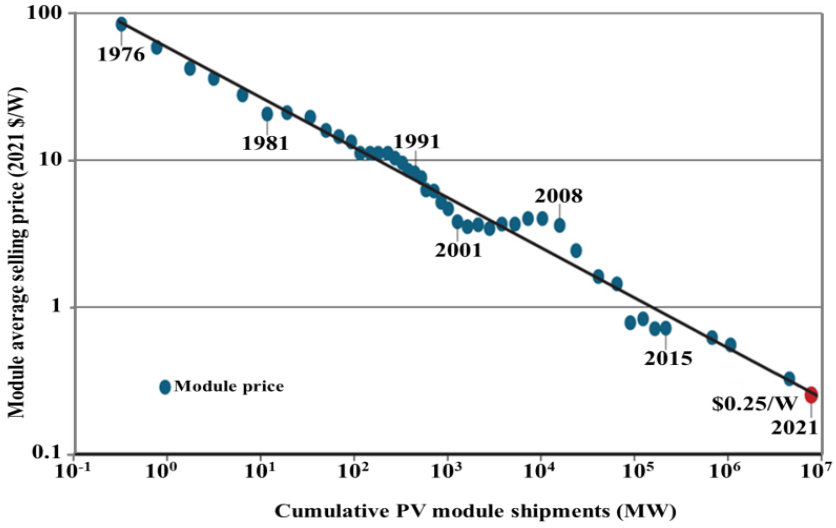

Figure 1.2 The ITRPV price trend of c-Si solar modules in US$/Watt$_p$ (ITRPV, 2022).

The second generation are based on thin-film solar cells with direct band gap absorber materials such as poly Si (pc-Si), microcrystalline Si (μc-Si), amorphous Si (a-Si), cadmium telluride (CdTe), copper indium gallium diselenide (CIGS) and copper zinc tin sulfide (CZTS) (Ushasree and Bora, 2019). The thickness of the absorber material in the second generation solar cells ranges from 1-5 μm (Selmane et al., 2022). The film solar cells are deposited on foreign substrates such as glass or flexible plastic, using various deposition techniques such as physical and chemical vapour depositions (Girtan and Negulescu, 2022; Wang et al., 2022). Thin film solar cells demonstrate efficiencies around 10-15%, as shown in Figure 1.3. The third generation consists of organic materials such as polymer, dye-sensitized and perovskite solar cells (Valadi et al., 2021). The deposition of these semiconductor materials can be done at low temperature on flexible substrates, which enables low technology cost and wider integration onto various surfaces (Lang et al., 2021). The thickness of the perovskite layers in the third generation solar cells ranges below 1 μm (Roy et al., 2022). However, one of the disadvantages of these materials is their instability in the operation environment, where the conversion efficiency of the solar cells can degrade in a matter of minutes or hours (Green et al., 2021; Valadi et al., 2021). As of 2021, the organic and perovskite solar cells exhibit efficiencies of up to 18.2% and 25.5% respectively (Wilson et al., 2020), as illustrated in Figure 1.3.

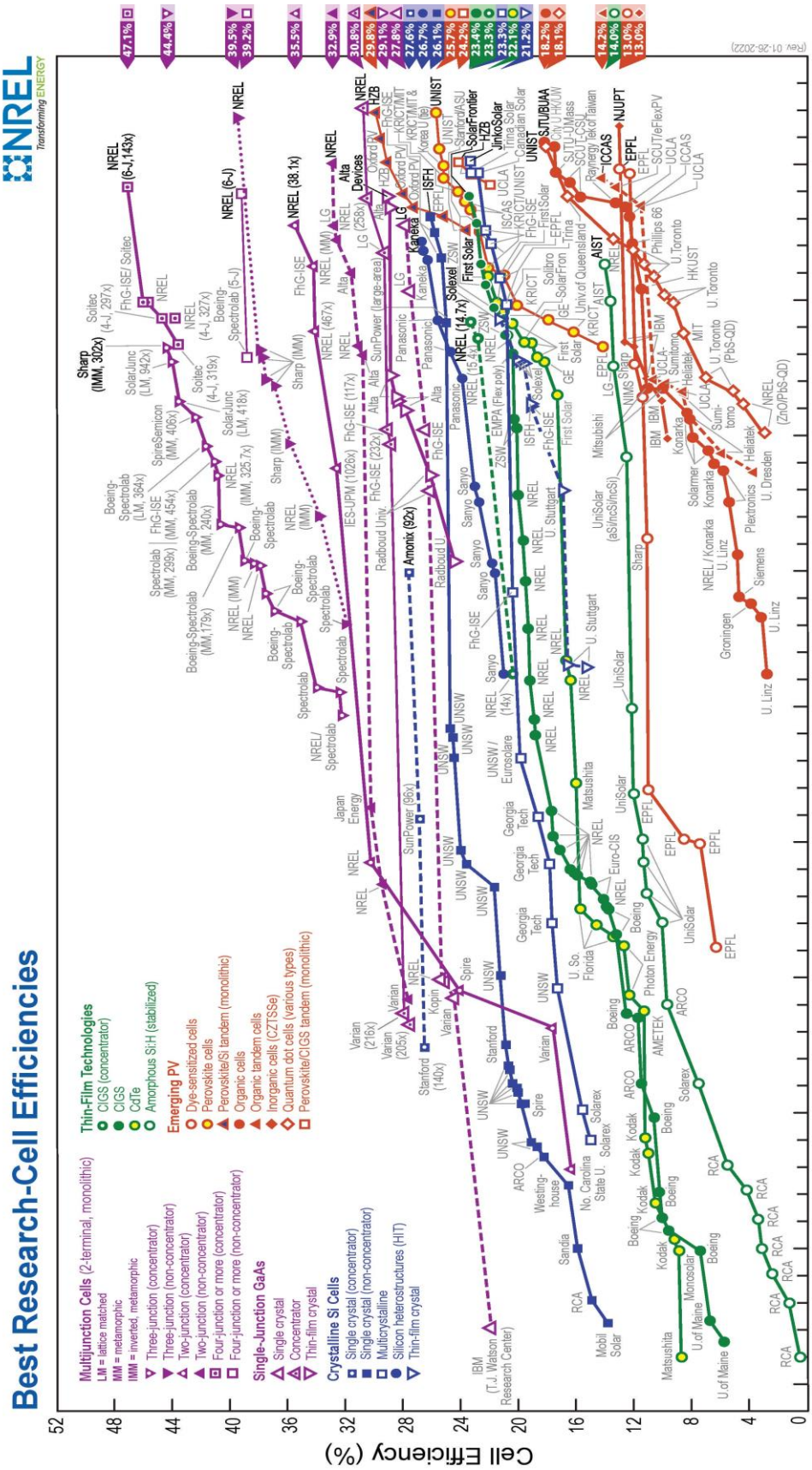

Figure 1.3 National Renewable Energy Laboratory (NREL's) best research solar cell efficiencies for different technologies, since 1975 (NREL, 2022).

1.2 Problem statement

The semiconductor material employed in most of today's solar cells is based on c-Si wafers. Planar c-Si wafers exhibits a high broadband reflection of about 35% over 300-1100 nm wavelength region (Da et al., 2018). This is due to the difference between the refractive indices (n) experienced by the incident light when travelling from air (n=1) into bulk c-Si material (n=3.94 at 600 nm) (Huang et al., 2022; Katiyar et al., 2015). Reducing the thickness of the c-Si wafer to below 100 μm causes the c-Si wafer to be flexible in shape. Apart from the cost of the solar cells consideration, thinner wafers can potentially lead to a higher open circuit voltage (V_{oc}) due to the lower bulk recombination and lower series resistance. This is because the photogenerated carriers do not need to travel a long distance (due to the thinner wafers) before being collected by the p-n junction. As a result, enhanced carrier extraction is achieved in the device. However, c-Si is an indirect semiconductor and therefore exhibits poor light absorption which results in low photocurrent from the solar cell (Hwang et al., 2018). In order to retain the light absorption in the flexible c-Si wafers, effective light management strategies are required over a broad wavelength range of interest in the solar cells (Hwang et al., 2020).

To overcome the poor light absorption in the flexible c-Si, black silicon (b-Si) could be a promising solution, which leads to excellent light coupling and superior light absorption within the 300-1100 nm wavelength region (Faro et al., 2019). To produce b-Si surface, metal-assisted chemical etching (MACE) technique is commonly employed due to its low-cost and facile fabrication process. B-Si involves modifying the planar surface of the c-Si wafer into a surface with dense nanowires (NWs) (Naffeti et al., 2020). This NWs layer is equivalent to a lower refractive index

(n) material. The b-Si NWs leads to a gradual change in n from air (n=1) to b-Si (n=2.43), and then to bulk Si (n=3.94) (Katiyar et al., 2015). In this thesis, silver (Ag) is used as the metal catalyst in MACE due to its stability in acids, exhibits fast etching rate, high redox potential, and non-oxidation during the MACE process (Alhmoud et al., 2021). Flexible b-Si wafers are brittle and fragile in nature and easily broken (Hwang et al., 2018). Besides, the flexible b-Si also suffers from low long wavelength light absorption. This is because the absorption in the near infrared (NIR) region of the solar spectrum is significantly reduced when the c-Si wafer thickness is reduced. To solve these challenges, a mechanically supporting substrate such as stainless steel (SS) or polyimide (PI) substrate is required to hold the flexible b-Si absorber on the rear side (Sivaramakrishnan Radhakrishnan et al., 2019). Both SS and PI substrates can also help to reduce transmission loss at the back of the flexible b-Si by interfacial reflection at the b-Si on SS or PI interface (Sharma et al., 2014; Wang et al., 2014). To further enhance the light absorption in the flexible b-Si absorber, the surface of the substrate can also be textured. The textured SS or PI substrate is expected to induce light scattering at the b-Si on SS/PI interface, leading to optical path length enhancement and improved light absorption in the b-Si absorber (Fortes et al., 2018).

Conventional b-Si solar cells utilize a high-temperature diffusion process (900-1000 ^{o}C) which involves a high thermal budget in order to introduce a thin diffused emitter for p-n junction formation (Ray et al., 2021). After the high-temperature diffusion process, the nanotextures could be deformed, which leads to increased broadband reflection and therefore reduced light absorption within the 300-1100 nm wavelength region (Stilling-Andersen et al., 2018). This issue can be mitigated by adopting an organic material such as PEDOT:PSS to form the front

emitter in a heterojunction solar cell configuration. Besides preventing the deformation of the nanotextures during the diffusion process, the PEDOT:PSS also reduces thermal budget due to its low process temperature requirement (100-200 ^{o}C) apart from being facile in nature (Zhang et al., 2017).

1.3 Objectives of research

The objectives of this work are as the following:

1. To characterize flexible b-Si prepared by silver-assisted chemical etching process.
2. To investigate the properties of textured SS and PI substrates at the rear side of the flexible b-Si absorber.
3. To study the properties of PEDOT:PSS emitter on flexible b-Si.
4. To assess performance of flexible b-Si solar cells on textured substrates in comparison to solar cells on untextured substrate.

1.4 Thesis outline

This thesis contains five chapters. Summary of the content of each chapter of this thesis is outlined as below. Chapter 1 provides the introduction about the various types of solar cell, problem statement, and research objectives are also outlined in this chapter.

Chapter 2 explains background information about flexible mono c-Si solar cells, light management such as light coupling, scattering and back surface substrate to minimize optical losses in flexible absorber. Besides b-Si fabrication methods and the mechanism behind the one-step MACE process that has been employed in this research are explained. At the end of this chapter, fabrication methods and characterizations of flexible b-Si solar cell are presented.

Chapter 3 includes the materials and techniques used for fabrication of flexible b-Si by one-step MACE process. This chapter also includes the principle of equipments in use to fabricate and characterise the surface morphologies, optical and electrical properties of the samples.

Chapter 4 presents results of the flexible b-Si wafers by one-step MACE technique with different etching durations and etchant volume ratios. Surface morphological and optical characterizations of the samples are evaluated. The effects of the SS and PI texturing towards absorption enhancement and maximum potential short-circuit current density ($J_{sc(max)}$) enhancement in the flexible b-Si is discussed. At the end of this chapter, electrical properties of the PEDOT:PSS/flexible b-Si solar cell on the textured PI are investigated.

Chapter 5 concludes and summarizes of the main findings and the original contributions of this thesis to the area of the flexible b-Si on SS and PI substrates. Besides, the recommendations for future work are also discussed at the end of this chapter.

CHAPTER 2

THEORETICAL BACKGROUND AND LITERATURE REVIEW

2.1 Introduction

This chapter introduces some background information for better understanding of the thesis. In this chapter, the motivation for flexible mono c-Si solar cells and optical properties will be discussed. The chapter also introduces the concept of light management for enhancing light absorption. The main focus is on b-Si by one-step MACE process and electrical properties optimization for homojunction and heterojunction solar cell applications. Finally, electrical properties of solar cells are presented.

2.2 Solar irradiation

The sun is the source of solar energy. This energy is radiated over a wide range of wavelengths (covering all visible plus part of ultraviolet and infrared). All of these radiations constitute the solar radiation characterized by its irradiance or spectrum (Ushasree and Bora, 2019). The solar irradiance or sunlight intensity is the spectral distribution of electromagnetic radiation as a function of the wavelength or equivalent of its frequency (Zhao et al., 2019). Irradiance refers to the amount of energy from the solar radiation perceived per unit area at atmospheric or ground level. It is expressed in W/m^2. After traveling a distance of about 150 million kilometers, the solar radiation arrives outside the atmosphere with an irradiance of about 1367 W/m^2 and it depends on the weather conditions (Ushasree and Bora, 2019). The solar spectrum is reflected or absorbed by gas molecules and dust particles such as water vapor (H_2O) and carbon dioxide (CO_2) present in the atmosphere, as shown in Figure 2.1.

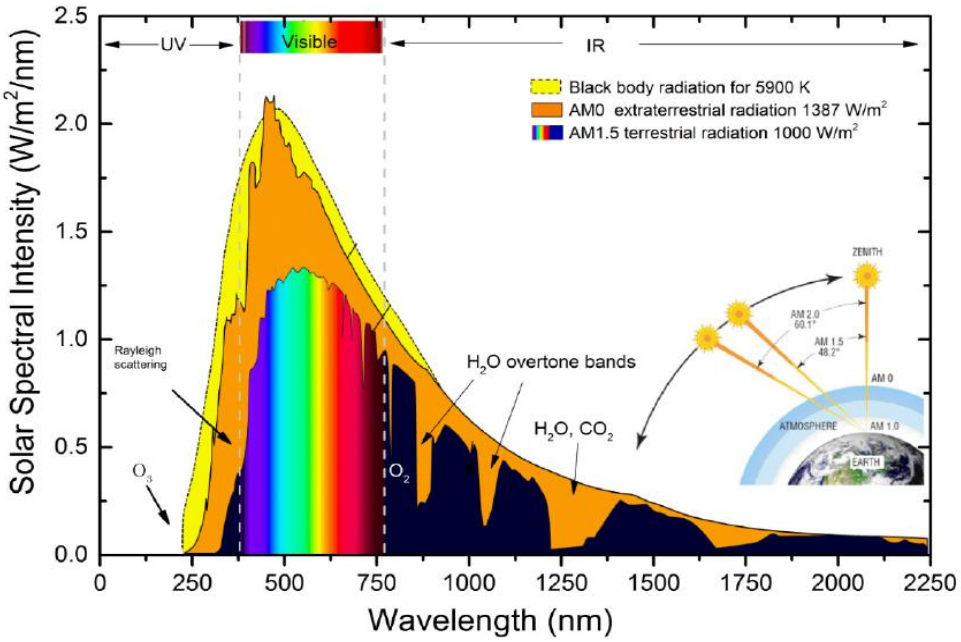

Figure 2.1 Spectrum irradiance for the standardized solar spectra. The figure is adopted by National Renewable Energy Laboratory (NREL) (NREL, 2022).

The attenuation of the solar irradiation varies depending on the path length of the route gone through by it to arrive at ground level. This path length depends on the position of the sun in relation to the zenith and is expressed in terms of air mass (AM). The AM can be calculated by using Equation 2.1. In Equation (2.1), θ is the angle between horizontal plane of the earth and solar radiation (Lipovšek et al., 2022).

$$\mathrm{AM} = \frac{1}{\cos\theta} \tag{2.1}$$

The solar spectrum in space (outside the atmosphere) therefore corresponds to the AM0. An AM1 is the sunlight after crossing of the atmosphere at 0^{o} zenith angle as depicted in Figure 2.1. In Table 2.1, the relationship between the AM and zenith angle is demonstrated. In the field of PV, standard test conditions (STC) is used to characterize and compare the performance of solar cells. This involves spectrum of AM1.5G (global) (θ=48.2^{o}) at irradiance of 1000 W/m^2 and temperature of 25 ^{o}C.

Table 2.1 Relationship between AM and zenith angle.

AM	Zenith angle (θ)
AM 0	–
AM 1	0
AM 1.5	48.2^{o}

2.3 Flexible monocrystalline silicon solar cells

This thesis is focused on flexible mono c-Si solar cell. Current PV technology is dominated by wafer-based c-Si cells. To reduce the technology cost of the solar cell, one promising strategy is by reducing the thickness of the c-Si material consumption to fabricate the solar cells since the c-Si wafers contribute over 50% of the total solar cell cost (Yu et al., 2016). Thin substrate is widely used for different applications since it enables flexible or bendable substrate, light-weight and creates new possibilities for flexible solar devices, as shown in Figure 2.2 (Costa et al., 2019; Tang et al., 2019; Um et al., 2021). Furthermore, lower c-Si thickness increases open-circuit voltage (V_{oc}) due to the lower series resistance and bulk recombination (Dai et al., 2019). To fabricate various thin c-Si wafers thickness, c-Si wafer has been etched using potassium hydroxide (KOH) solution at different etching times (Wang et al., 2013). However, the thickness reduction leads to efficiency penalty, since flexible c-Si wafers result in incomplete light absorption, leading to lower short-circuit current density (J_{sc}) in the solar cells (Hwang et al., 2018). In the literature, thin c-Si wafers have been used to fabricate heterojunction solar cells for different thickness c-Si (60 and 125 μm) was used. The external quantum efficiency (EQE) curve of the 60 μm-thick solar cell is lower if compared to the 125 μm-thick solar cell due to poorer light

absorption in the thinner solar cell. This leads to a corresponding decrease in J_{sc} to 36.9 mA/cm^2 (or 2% reduction compared to the 125 μm-thick cell) (Augusto et al., 2016). In another study, the average reflection for 180 μm-thick is lower above 800 nm when compared to the thinner wafer thickness (with 65 μm-thick) due to higher escape reflection in the thin c-Si wafers (Do et al., 2014). In general, the power conversion efficiency (η) of the wafers decreases when the wafer thickness is reduced to below 100 μm due to the reduction of the J_{sc} at the longer wavelength and the same effect already has been reported (Dai et al., 2019; Hwang et al., 2018). The details will be presented in Section 2.9.

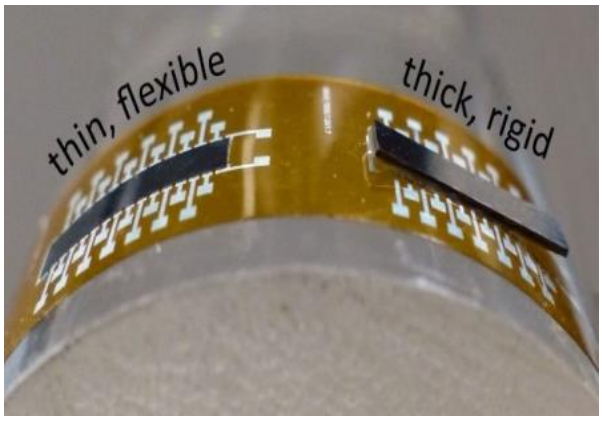

Figure 2.2 Flexible device on a plastic substrate that ensures mechanical stability (Zhang et al., 2022).

2.4 Optical properties of flexible monocrystalline silicon

The schematic of the planar c-Si wafers with thickness of about 180 μm and lower than 70 μm is shown in Figure 2.3. For both thicknesses, planar c-Si exhibits a high broadband reflection of about 35% over 300-1100 nm wavelength region due to the incident light reflected at the air-flexible c-Si interface (Da et al., 2018). C-Si wafers with 180 μm thickness are usually used for solar cell manufacturing and reduction in the thickness of c-Si wafers would be desirable to reduce the cost

(Andreani et al., 2019). With 180 µm, the long wavelength light (particularly above 800 nm) represents a transmission loss. When the thickness of c-Si wafers is reduced, more and more long wavelength light is transmitted. Reducing the thickness of the c-Si to below 70 µm compromises its light absorption capability, due to increased light transmission loss (above 800 nm) (Sivaramakrishnan Radhakrishnan et al., 2019). This indicates that the main optical absorption loss for a flexible c-Si solar cell is due to the high front reflection and transmission loss suffered by the thin c-Si in the long wavelength region. In the NIR region, thinner wafers exhibit higher transmission (red light transmission was observed when the 6.8 µm thick c-Si wafer was illuminated by a white light, as shown in Figure 2.4). From the reflection (R) and transmission (T) results, absorption (A) is determined by A= (100–R–T)% (M. Li et al., 2021).

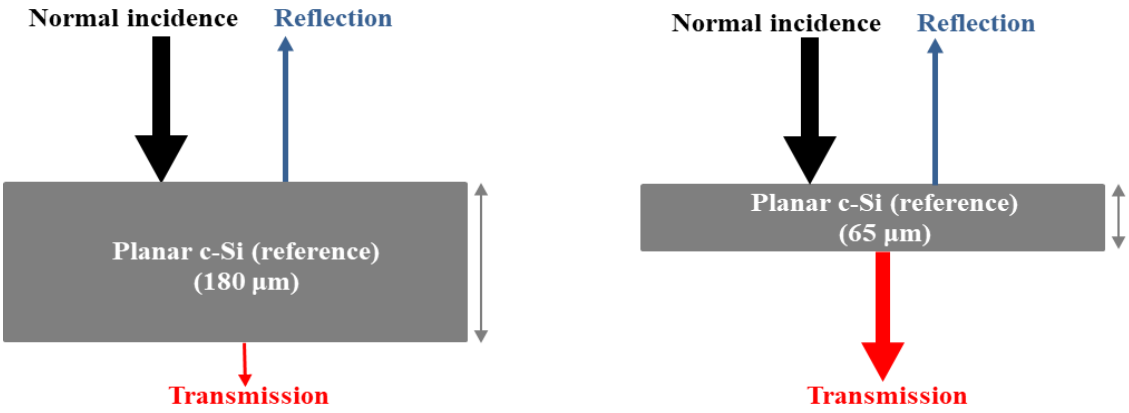

Figure 2.3 Path of the incident light upon incidence (left) planar c-Si (180 µm thickness) and (right) planar c-Si (65 µm thickness). Note that the diagrams are not to scale.

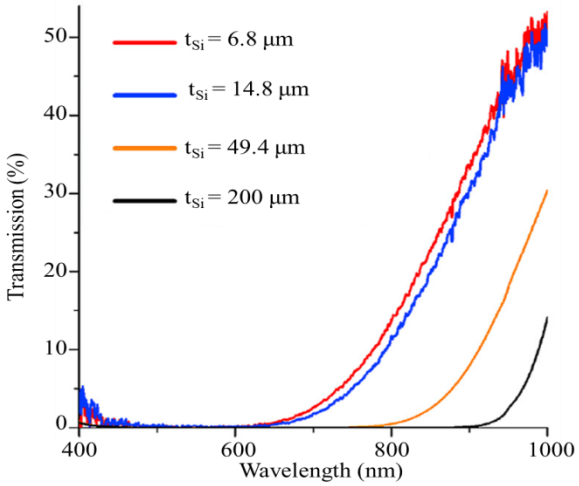

Figure 2.4 Transmission spectra of c-Si wafers with thicknesses of t_{Si}=6.8, 14.8, 49.4, and 200 µm (Dai et al., 2019).

C-Si is a poor light absorber, due to its indirect band gap nature (Yuan et al., 2018). In an indirect band gap semiconductor, the maximum of valence band (VB) and the minimum of conduction band (CB) have a different value of electron crystal momentum (k), as depicted in Figure 2.5. This crystal momentum difference leads to extra phonon required to enable electron transition from VB to CB during light absorption in the c-Si.

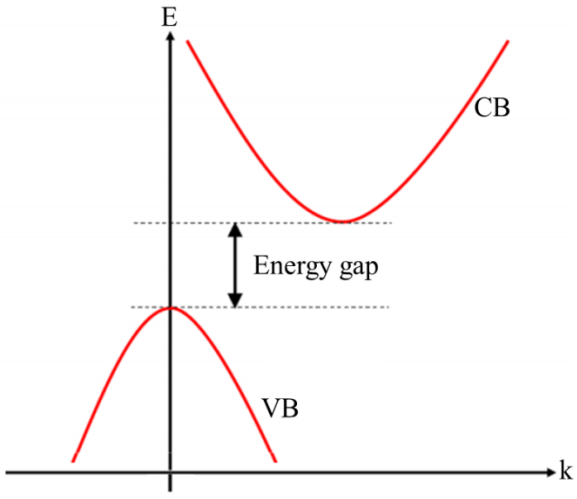

Figure 2.5 E-k diagram of c-Si (Yuan et al., 2018).

In Figure 2.6, c-Si demonstrates low absorption coefficient in the NIR region. As a result, thickness of less than 70 μm will be insufficient to absorb the incident light, which leads to reduced light absorption hence low photocurrent in the solar cells.

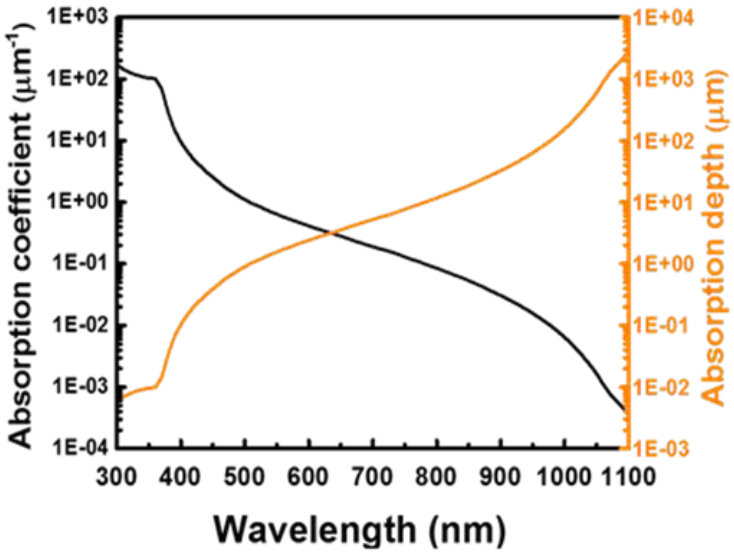

Figure 2.6 Absorption coefficient and absorption depth of c-Si at 300 K (Hwang et al., 2018).

In industrial mono c-Si solar cells, light management strategies are incorporated by texturing the front surface of the solar cells with random pyramids in a wet chemical solution which scatter the incident light into oblique angles, resulting in lower broadband reflection and improved light absorption within 300-1100 nm wavelength region. Apart from the above approach, a thin layer of anti-reflection coating (ARC) such as silicon nitride (SiN_x) with refractive index (n) of about 2.0 at 600 nm and standard thickness of 75 nm is deposited on the front pyramids by plasma enhanced chemical vapour deposition (PECVD) technique (Chang and Sun, 2018; Zin et al., 2018). However, there is still considerable reflection loss experienced by the solar cell after the ARC deposition (Scheul et al., 2022). In the past decades, various

strategies have been proposed to improve conversion efficiencies in solar cells. In this thesis, to overcome the challenges in the flexible c-Si, many approaches will be explored and implemented. The main strategies to reduce the optical reflection and transmission resulting in increased absorption. One strategy involves the creation of b-Si nanotextures and the other requires the use of rear supporting substrate with a back reflection such as SS or plastic substrate (Sivaramakrishnan Radhakrishnan et al., 2019; Wang et al., 2014; Weisse et al., 2012). In the following sections, an efficient light management strategy to retain the same level of light absorption and photocurrent in the solar cells will be explained.

2.5 Light management in flexible monocrystalline silicon solar cells

Light management involves all the techniques such as light-coupling, scattering and total internal reflection which aims to minimize the optical losses in the flexible c-Si absorber (Barugkin et al., 2016). Light management is particularly important for a flexible c-Si absorber (especially below 100 μm) due to incomplete light absorption (Um et al., 2021). To increase the light-coupling into flexible c-Si absorber, it is important to reduce on the front surface reflection losses. Nanostructure is a promising way to minimize front reflection of flexible c-Si cells, which can be attributed to refractive index grading effect at the air and nanostructured Si interface (Gaudig et al., 2018).

Furthermore, it is important to note that the flexible c-Si at thickness below 100 μm is fragile and easily broken. The supporting substrate such as stainless steel (SS) and polyimide (PI) can be used at the back of absorber material. Beside, being a strong mechanical support, the SS and PI substrate can also act as a rear reflector that reflects the light back into the absorber material and prevent transmission loss of the

long wavelength light (particularly above 800 nm) (Sharma et al., 2014). With the increased rear reflection and reduced transmission loss, light absorption in the thin absorber material can be improved significantly. To further enhance the light absorption, the surface of the SS or PI substrate can be textured. The texturing aims to produce surface roughness on the SS and PI surface, which could enhance light scattering (i.e. multiple-passes of the incident light through the thin absorber layer) at the rear side of the absorber layer (Ingenito et al., 2014). The enhanced scattering is expected to improve light absorption in the absorber layer, leading to the increase optical path length enhancement and improved absorption in the absorber layer (Catchpole and Polman, 2008).

Total internal reflection occurs when the scattered light with angles larger than the critical angle of the interfaces (Ingenito et al., 2014). The above light management techniques improve broadband light absorption in the thin absorber layer. Another possible way to reduce optical loss is by using metal nanoparticles (NPs) for a thin c-Si solar cells since they can play the double role of back reflector (BR) and rear electrode (Sharma et al., 2014). Besides, the textured metal reflector increases the absorption due to parasitic surface plasmonic losses and enhanced light scattering at the textured interface. However, Ag BR is an expensive material, which needs costly equipment for fabrication. In the following sections, this light management techniques will be reviewed and how they lead to the absorption enhancement in the flexible b-Si will be explained.

2.6 Black silicon

B-Si is a promising candidate to reduce technology cost while maintaining superior broadband light absorption within 300-1100 nm wavelength region. B-Si

involves modifying the planar surface of the c-Si wafer into a surface with nanostructures (Huang et al., 2022). The optical properties of b-Si surface strongly depend on the surface morphology and the colour of the surface changes from silver for planar c-Si surface to black for b-Si, as in Figure 2.7 (a,b) (Chai et al., 2020). The b-Si contains random nanostructures on the surface of c-Si wafers without additional ARC, which results in the suppression of broadband reflection from ultraviolet (UV) to infrared (IR) regions (Hsu et al., 2020). The energy band structure of c-Si is changed to enable the absorption of photon energy below the forbidden bandwidth, and light absorption in the range of 1100-2500 nm exceeds 90% (Fan et al., 2021). The refractive index depends strongly on the depth and length of the nanostructure and other geometrical properties. For example, if the b-Si NWs array has a base diameter of NWs of 150 nm and height of 300 nm. The b-Si surface appears as a homogenous medium with a gradual change of n when the incident light travels from air (n=1) and n b-Si NWs varies smoothly which reaches a value of ≈ 2.43 and then to bulk c-Si, as illustrated in Figure 2.7 (c). The refractive index gradient in the b-Si NWs is shown to play an important role to suppress the resulting reflection (Katiyar et al., 2015).

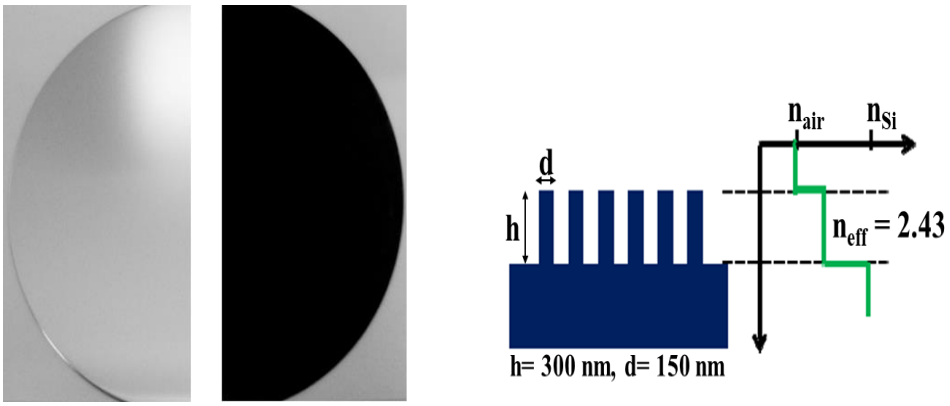

(a) (b) (c)

Figure 2.7 (a) Planar c-Si wafer (b) black silicon wafer (Zhang et al., 2020) (c) schematic diagram of b-Si NWs in the corresponding effective refractive index (n_{eff}) when the incident light travels from air (n=1) into bulk c-Si (n=3.94) (Katiyar et al., 2015).

With the b-Si surface, the longer length of NWs in a solar cell reduces the reflection of light, but at the same time, the recombination loss increases due to higher surface defects, and the cell efficiency is decreased (Sahoo and Kale, 2019). The surface recombination can be reduced by reducing the density of surface states or by reducing the concentration of free electrons or holes at the surface. A passivation layer is one possible solution for reducing surface recombination. The concentration of free electrons or holes at the surface can be reduced by the formation of an internal electric field below the semiconductor surface. Besides electric field effect can also be created from a passivation layer (Chai et al., 2020). There are various materials including SiN_x, silicon dioxide (SiO_2), titanium oxide (TiO_2) and aluminium oxide (Al_2O_3) and several techniques that are suitable for passivation of the surface including atomic layer deposition (ALD), sputtering and wet chemical for deposition of a passivation layer (Huang et al., 2022). ALD is one of the most promising techniques because of the conformality on the nanostructured surfaces and good thickness control (Pasanen et al., 2017). The passivation layer can contain one material in a single layer or combine different materials in a multi-layer configuration. The effiency solar cell is highly dependent on the thickness of the passivation layer. A thick layer can damage the optical effect, but it must be thick enough to get the effect of a surface passivation layer. The schematic illustration of Al_2O_3 ALD is deposited on b-Si solar cell, as depicted in Figure 2.8. Recently, b-Si was fabricated by deep reactive ion etching and nanopillars with lengths of about 800 nm were formed on the wafer surface. The effective minority carrier lifetime in b-Si was significantly increased by one order of magnitude with the Al_2O_3 (about 20 nm) passivation layer due to the suppressed surface recombination (Savin et al., 2015).

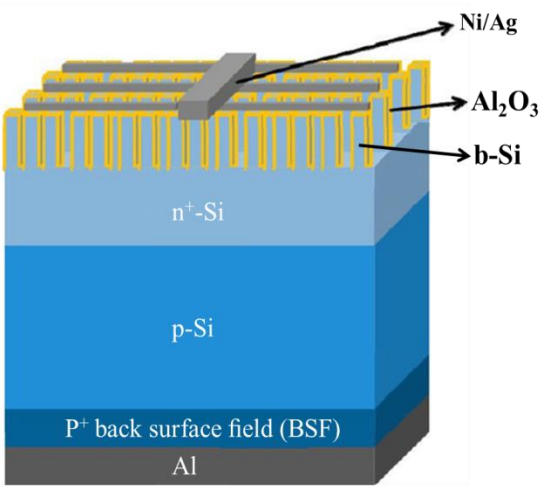

Figure 2.8 Schematic diagram of Al_2O_3 surface passivation on b-Si solar cell (Wang et al., 2013).

2.7 Fabrication of black silicon

In the recent decades, ranges of b-Si fabrication process have been developed. B-Si can be fabricated using several techniques, including dry etching process like reactive ion etching (RIE), femtosecond laser irradiation and wet etching process like electrochemical etching and MACE (Chai et al., 2020). Nanostructures present on the surface of the wafers are usually NWs, nanopores or nanocones with various lengths and diameters, depending on the type of the techniques, as well as the parameters used in the methods (Chai et al., 2020). The fabrication techniques of b-Si are briefly introduced below.

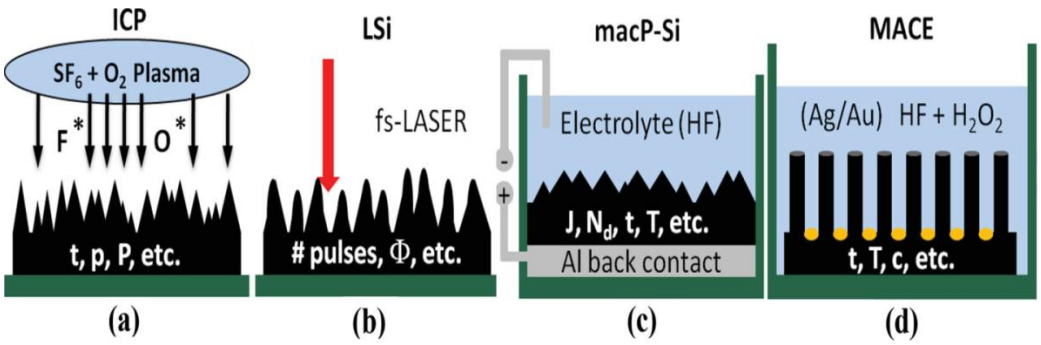

Figure 2.9 Cross-sectional schematic diagrams of the b-Si using different fabrication techniques such as (a) RIE process in an atmosphere of SF_6 and O_2 (b) needle-shaped structures by femtosecond laser pulses (c) macroporous Si fabrication by electrochemical etching (d) MACE process with Ag/Au catalyst NPs in aqueous HF and hydrogen peroxide (H_2O_2) solution (not to scale) (Otto et al., 2015).

The use of RIE to form micro-grass on the surface of the wafer was first studied by Jansen in 1995, as shown in Figure 2.9 (a). The RIE technique employs with gases mixture of sulphur hexafluoride (SF_6) and oxygen (O_2). During SF_6 and O_2 the etching process, F^* radicals help in the formation of silicon-oxyfluorine SiF_4:O_2 plasma that produces O^* radical to help the passivation with SiO_yF_z. Etching the surface of wafer, using SF_6 at low pressures and temperature, is used to fabricate anisotropic etch profile. The b-Si morphology depends on the applied process parameters such as time and pressure. However, the cost of RIE technique is expensive due to requirements of experimental setup (Hsu et al., 2014).

Eric Mazur and his team discovered a novel technique for fabrication b-Si in 1998. The wafer was mounted on a motorized two-axis translation stage inside a vacuum chamber. The laser induced cones in c-Si wafers were produced as micro-sized spikes structures using nanosecond ultraviolet laser pulses, as illustrated in Figure 2.9 (b). Recently, thin c-Si with thickness 30 μm has been used to fabricate thin b-Si by femtosecond laser. Micro spikes are formed on the b-Si surface after the laser illumination (Mei et al., 2011). The characteristics of the micro-sized spikes depend

on the irradiation intensity, spot size, number of pulses and ambient environment. However, this technique is not suitable for manufacture due to the expensive laser instruments required (Sarnet et al., 2008).

Another process to fabricate the b-Si is by electrochemical technique, which involves a c-Si wafer tied to the anode of an electrochemical cell, immersed in a solution containing hydrofluoric acid (HF), deionized water (DI H_2O) and ethanol, as shown in Figure 2.9 (c). The mechanism of the reaction, the etching process is initialized by applying a voltage bias or a current. Based on the current density, the process can occur in three regions such as low, high and transition current density regions (Liu et al., 2014). In this technique, the morphological properties of the b-Si depend on c-Si wafer doping type and dopant concentration. The basic techniques employed to control the parameters are illumination, etching time and current density.

Another common method to fabricate b-Si is by MACE technique. The wafer is etched in the presence of noble metals and HF acid with oxidizing agent, to form nanostructured on the wafer surface, as shown in Figure 2.9 (d). The MACE process was first proposed in 1997 by Dimova-Malinovska (Huo et al., 2020). In the etching process, a wafer is partly covered by metal NPs and dipped in a aqueous solution of HF acid with an oxidizing agent. Ag and Au are the most popular noble metals candidates due to their resistance to degradation. Other catalysts being investigated are nickel (Ni) and copper (Cu). In the next section, fabrication of b-Si by MACE process will be explained in more detail.

A recent study on MACE technique has been carried out by Nichkalo et al. to fabricate nanograss on c-Si (111) wafer by dipping the wafer in aqueous solution of HF (5 M) and $AgNO_3$ (2 mM) for 2 min and then etching in HF:H_2O_2:DI H_2O at room

temperature for 10 min. From the process, random nanograss with average height of about 4 μm is formed. This results in reflection of about 4% at wavelength of 600 nm (Nichkalo et al., 2018). In recent study on two-step MACE process, Ag NPs have been deposited on c-Si surface, and the wafers were immersed in solution containing of $AgNO_3$/HF (0.02/4.6 M) for 2 min at room temperature, followed with 3 min etching in HF/H_2O_2 (4.5/0.15 M). From this process, Si NWs with diameter of 64–240 nm and length of about 2 μm are formed. This leads to reflection of less than 10% at wavelength of 600 nm (Nichkalo et al., 2017). Apart from using Ag as the catalyst to fabricate flexible b-Si, Au NPs (with 10 nm thickness) have been used by (Kumar et al., 2019). In their work, c-Si wafers are etched in H_2O_2:HF (2:1 vol. ratio) for 5 min and 10 min respectively. The b-Si produces diffuse reflection of less than 1% within 200–800 nm wavelength range. In other work, ultra-thin b-Si (with 10 μm thickness) has been fabricated using combination of silica (SiO_2) nanosphere lithography and MACE technique. The flexible b-Si solar cell exhibits conversion of 4.3% when compared to the planar mono c-Si solar cell (with efficiency of 3.2%), owing to lower reflection and improved light absorption in the flexible b-Si solar cell (Roy et al., 2016).

2.8 Metal-assisted chemical etching (MACE)

Among the aforementioned methods, MACE technique is widely investigated because it is facile, requires simple setup and low-cost in nature (Srivastava and Khang, 2021) since mass production of PV cells is focusing on reducing the amount of material used and fabrication cost. This offers a significant advantage over RIE process which requires vacuum processing and complicated setup. Besides, RIE is also more expensive since it requires state of the art processing equipment (Fan et al.,

2021). However, MACE of c-Si is considered as electrochemical by using catalytic reaction. MACE technique can be divided into one-step and two-step processes. The effect of the crystallographic orientation of the substrate on MACE depends on the reaction conditions. Peng et al. (Peng et al., 2005) reported on fabrication of Si NWs perpendicular to the surface using wafers with (100) and (111) crystallographic orientations. Other factors that affect the nanostructures on the wafer surface include etching time, etchant concentration, annealing temperature and type of metal catalyst (Huo et al., 2020).

2.8.1 One-step and two-step MACE processes

In one-step process, c-Si wafers are dipped in aqueous metal salt solution such as silver nitrate ($AgNO_3$), tetrachloroauric (III) acid ($HAuCl_4$) and hexachloroplatinic (IV) acid (H_2PtCl_6) with hydrofluoric (HF) acid at room temperature with an oxidizing agent such as H_2O_2 (Matsumoto et al., 2020). The role of oxidizing agent is to increase the reaction rate of holes injection into the c-Si wafers. During this process, deposition of NPs and etching of c-Si surface take place at the same time. In a recent study, c-Si wafers with thickness of about 280 μm have been used to fabricate b-Si NWs by one-step MACE process in aqueous solution containing 60 ml of HF (49%) and 50 ml of $AgNO_3$ for a duration time between 60 and 90 s, and NWs with lengths of about 2.0–2.9 μm are formed. As a result, absorption of 94% is obtained at wavelength of 600 nm (Abdulkadir et al., 2019).

On the other hand, in two-step process, metal NPs such as Ag and Au are deposited either by aqueous solution or physical deposition such as sputtering, followed by etching in an aqueous solution of HF acid, H_2O_2 and DI H_2O at room temperature. For fabrication of flexible b-Si, two-step MACE process has been used by Kumar et al. to fabricate NWs on flexible c-Si wafers by a thin layer of Au NPs is